Research Article

Application of UAV Remote Sensing Technology in the Construction of Modern Smart Farm

Tiantian Zhang, Dongha SHIM ⓘ, and Jae-sang Cha

Seoul National University of Science and Technology, Seoul, Republic of Korea

Correspondence should be addressed to Dongha SHIM; ttdas@zju.edu.cn

This article is to study the application and optimization of UAV remote sensing technology in the construction of smart farms. Multiparty calculations, circuit design, remote sensing, and remote control are used wirelessly, with a wide field of vision and easy evasion. Its transmitting frequency, transmitting power, interference electromagnetic wave intensity, receiving sensitivity, and gain coefficient are all factors that affect wireless remote sensing. Stress and strain are also important factors for the timely response and control of remote sensing technology. This article first outlines smart farms and drones, and then describes how to design drone circuits. Its smallest UAV circuit design includes UAV reset circuit, UAV crystal oscillator circuit, UAV upgrade circuit, UAV PPM decoding module circuit diagram, and then explains the attitude calculation and complementary filtering of the multiwing UAV. The complementary filtering algorithm is applied to the attitude calculation, and the error is reduced through the analysis of the coordinate system, the quaternion method, and the calculation of Euler angles. Then establish a wireless communication propagation model for smart farmland monitoring. Among them, the Egli model is selected. After data monitoring, it is obvious that the Egli model can monitor higher path loss, higher accuracy, and stronger propagation strength. Then through experiments, the static data of the two different tail transmissions under different loads are analyzed, the stress-strain trend line is observed, and the performance of the two transmission systems is analyzed. It can be seen that under the same conditions, the bevel gear tail transmission system has higher comprehensive performance, good reaction force characteristics, and excellent stress-strain performance. The power ratio of the synchronous belt tail drive system is 31.22, and the power ratio of the bevel gear is 29.52, a difference of 5.76%. The power ratio wind speed value of the tail part of the timing belt is 0.01014, and the power ratio wind speed value of the bevel gear is 0.009851, a difference of 2.93%.

1. Introduction

The UAV's wireless sensing mode and its lightness, high-altitude operation, wide vision, diverse functions, and compact size have been used in many ways. At present, the agricultural field is also closely following the sight of science and technology, making drones all over the wheat fields, rice, mountains, plains, and other scenes. The drone can spray evenly and spray pesticides on a large area, and after multiple calculations, the optimal concentration can be set, so that the vegetation in the smart farm can be optimally treated. And it can measure the concentration of pheromone when the vegetation matures, vegetation humidity, temperature, whether there are pests, and whether they are diseased, and it can accurately avoid obstacles during the flight, and can shuttle freely in plains, hills, farmland, and mountains. And the path loss can be controlled to be low, with monitoring functions, capable of signal monitoring, and a good drone can predict natural disasters and reduce electromagnetic interference. In short, UAVs have great advantages in farm construction. Using UAV remote sensing technology to obtain ground farmland information can make up for the shortcomings caused by satellite remote sensing and conventional aerial photography. Its remote sensing, low-

altitude flight, GPS positioning, and other technologies have been applied to the monitoring of geological disasters. Under the conditions of crop growth and soil on the ground farmland, in-depth research on high-resolution farmland remote sensing images brings unlimited value to agriculture. This article first outlines smart farms and UAVs and then describes the design of UAV circuits, minimum UAV circuit design, UAV PPM decoding module circuit diagram, multiwing UAV attitude calculation, and complementary filtering; the complementary filtering algorithm is applied to attitude calculation; the wireless communication propagation model of smart farmland monitoring is established; and the Egli model is applied. Finally, the statics simulation experiment of the different tail transmission systems of the single-rotor agricultural UAV is carried out to analyze the statics data of the synchronous belt tail transmission system under different loads. It can be seen that the power point distribution and stress and strain, output and speed fitting, output and wind speed fitting, the comparison of the bevel gear tail drive system, and the synchronous belt tail drive system tail rotor. The gear tail transmission system has good dynamic characteristics of the reaction force and can be applied to intelligent construction farms. The experimental results have guiding, theoretical, and practical significance for the construction of remote sensing single-rotor agricultural drones for intelligent farms.

The application of UAV remote sensing technology in farms has extremely optimistic development prospects. All fields have never stopped the research and exploration of UAVs, so that UAV technology will be studied more deeply and be applied. Semkin demonstrated the quasisingle static radar cross-section measurement of different UAVs at 26-40 GHz. He studied the radar cross-section characteristics of nine different multirotor platforms and a single lithium-ion polymer battery. The measurement results confirmed that large drones made of carbon fiber are easier to detect, while drones made of plastic and styrofoam materials have lower visibility to the radar system [1]. Chang and his companions developed a new type of sampling vehicle, a multirotor drone with a remote-controlled integral air sampling device to collect aerial samples with high sample integrity and preservation conditions. Paired comparisons were made between aerial samples (300 meters high) and ground samples to examine the vertical mixing of trace gases at coastal sites under three different meteorological conditions: local circulation, frontal passage, and high-pressure peripheral circulation. Kawai said that virtual wireless LAN devices can use the default operating system driver to simulate wireless LAN communications. Network simulators and virtual machines also reduce node costs, reduce the burden of site preparation, and reproduce radio propagation by modeling the evaluation environment [2]. Chen uses a detection drone to photograph pests and uses the Tiny-YOLOv3 neural network model based on the embedded system NVIDIA Jetson TX2 to identify T. papillosa in the orchard, thereby determining the location of the pests in real time. Then plan the best pesticide spraying route for agricultural drones based on the location of the pests. In addition to optimizing the spraying of pesticides for drones, the TX2 embedded platform also transmits the location and occurrence of pests to the cloud and uses computers or mobile devices to record and analyze the growth of longan. A drone was used to investigate the damage to the farmland surface caused by the 2016 Kumamoto earthquake [3]. Ishitsuka uses SfM and MVS to process drone aerial images to make a 3D model and makes DSM by calibrating the altitude level together with the Geographic Survey Institute and ground measurement results. As a result, the amount of unevenness (difference from the average altitude of the farmland ground) can be measured [4]. In his work, Tassi introduced the derivation, design, and implementation of the discontinuous Galerkin finite element method (DGFEM) for sediment transport and bed evolution equations. The numerical morphological dynamic model involves the coupling between the hydrodynamic flow solver as the driving force and the bed evolution model that explains changes in sediment flux and water depth [5]. Hanson developed a finite element model by extending the previous flow plane model, which can solve the stress balance equation of three-dimensional glacier dynamics. The model retains all terms of the stress tensor and uses the Glen-type power law to calculate the viscosity. The model was applied to Storglaciären in Sweden to explore the dynamics of the glacier and the characteristics of the model [6]. Although this experiment has reached certain guiding conclusions, there are unavoidable errors, which need to be further improved.

This article analyzes the stress and strain performance of different transmission systems of UAVs, provides guidance on the application of remote sensing technology, and describes the circuit design methods of UAVs and what methods can ensure the safety of UAVs during flight. It also talked about the application of attitude algorithm, Euler angle, and quaternion in UAV electromagnetic sensing technology and established the Egli model of agricultural UAV. And through the comparison of the free space model, the Egli model is proved to be excellent. Finally, two transmission system tests of single-rotor UAVs were carried out, and it was determined that the bevel gear tail transmission system had higher dynamic characteristics than the tail rotor reaction force of the synchronous belt tail transmission system.

2. Method

2.1. Circuit Design Method of UAV Based on Remote Sensing Technology. The UAV flight control system refers to a control system that can stabilize the flight attitude of the UAV and control the autonomous or semiautonomous flight of the UAV. It is the brain of the UAV and the main symbol that distinguishes it from the aircraft model. It is referred to as flight control. The UAV flight control board is composed of circuit, motion sensor, electric drive system, wireless communication, and power supply. Its structure is shown in Figure 1.

2.1.1. Design of UAV's Minimum System Circuit. Its structure includes AD conversion filter circuit, reset and crystal
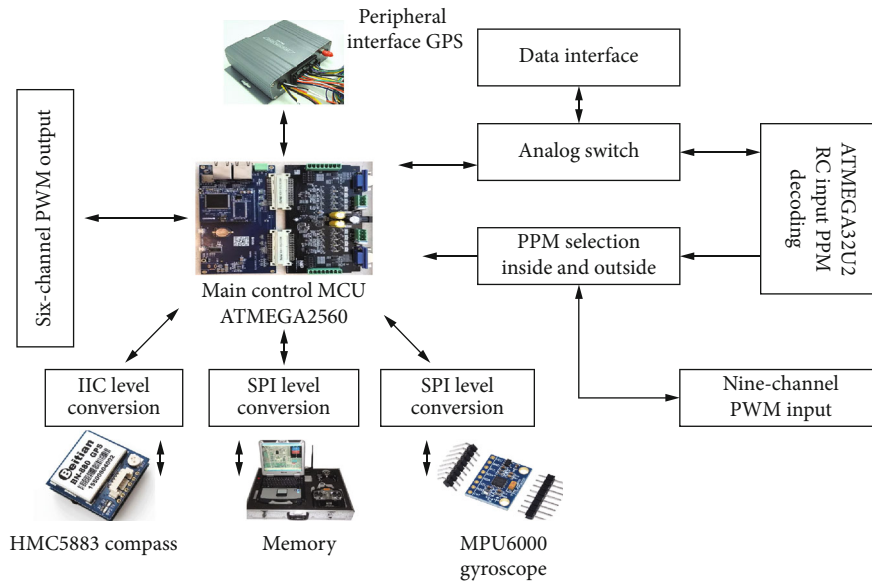
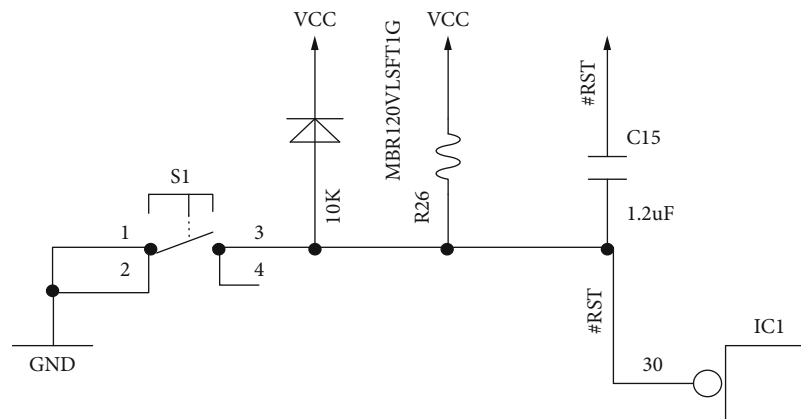FIGURE 1: Hardware structure diagram of UAV system.

FIGURE 2: UAV reset circuit.

oscillator circuit, ISP download interface, built-in power-on reset design, and control the redundant time during reset. Therefore, the circuit on the reset circuit outside the AVR only needs to be designed briefly, using a 10 K resistor and a 0.12 uF capacitor to resist interference and clutter. 1 N4148 can control the highest voltage. When the voltage is too high, the resistance reaches a certain value, which can cause a short circuit to protect the circuit [7]. When the AVR starts to work, turn on the switch to change the reset angle to low level, so that the AVR chip returns to its original position. When applied in reality, even if the reset pin is not allowed to touch any part, the AVR chip can operate as usual, as shown in Figure 2.

Mega2560 has built-in RC oscillator circuit, to get accurate baud rate, it can use an external crystal oscillator circuit. The influence of the crystal error on the baud rate is very small and can be ignored. This circuit can generate oscillation frequencies of 1, 2, 4, and 8. When Mega is used in reality, the capacitors can operate normally with-

out connecting to each other. In this article, we will connect it to ensure the standardization of the line. If the frequency accuracy obtained is not too high, it can also be connected to the internal RC oscillator, as shown in Figure 3.

The interface of the ISP download circuit does not require external parts, so the reset pin is not interfered by it. When used in reality, there is no need to weld 2 ∗ 3 seats, and this vacancy can be filled only with the AVR upgrade software, as shown in Figure 4.

2.1.2. PPM Decoding Module Circuit Diagram. This circuit has a monitoring function and can perform signal monitoring to switch the line opening and closing state, change the line at any time, and improve the safety of the UAV system, as shown in Figure 5.

2.2. Multiwing UAV Attitude Calculation and Complementary Filtering. Attitude calculation is very important for the flight
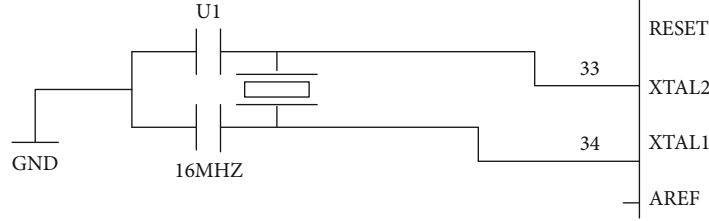
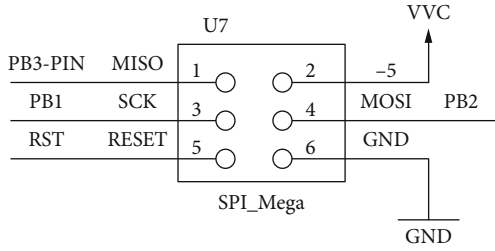FIGURE 3: UAV reset crystal oscillator circuit.

FIGURE 4: UAV upgrade circuit.

control system. The calculation process combines inertial navigation and sensor data fusion. The flight control board of the six-rotor UAV is equipped with a three-axis accelerator, barometric altimeter, magnetometer, and other sensors. Among them, the accelerometer has excellent low-frequency characteristics, can calculate the angle, with high accuracy, and is not affected by aging [8]. The three-axis gyroscope is subject to aging control, and the error value will increase if the time is too long. Applying the complementary filtering algorithm to the attitude calculation, the two sensors can be refined and discarded. After a certain period of time, use the accelerometer to calibrate the three-axis gyroscope, the calculated complementary filtering is its best state, and the average value is used in the calibration process [9].

2.2.1. Coordinate System Analysis. Taking the three-dimensional coordinate axis as the inertial reference system, set it to omxmymzm, which is the m system, and the body coordinate system to onxnynzn, which is the *n* system, and use Euler angle, quaternion, and cosine matrix to realize the mutual conversion between the two systems. Euler angles are not suitable for full attitude calculation. In

the attitude calculation and complementary filtering of the multiwing UAV, the Euler angle has the gimbal deadlock when solving the attitude, so it is not suitable for the full attitude. The quaternion method has a small amount of calculation, but it can be applied to the real-time motion calculation of hexarotor UAVs. The directional cosine algorithm is too cumbersome and has errors in real-time [10]. That is, it is can be used the quaternion method to calculate the process and the Euler angle to calculate the final output. Defining Euler's angle as the rotation angle, let the roll angle be θ_1, the pitch angle be θ_2, the yaw angle be θ_3, and the m-system rotation is the n-system, the three relations of zxy can be obtained as

$$Wx(\theta_1) = \begin{bmatrix} 1 & 0 & 0 \\ 0 & \cos(\theta_1) & \sin(\theta_1) \\ 0 & -\sin(\theta_1) & \cos(\theta_1) \end{bmatrix},$$

$$Wy(\theta_2) = \begin{bmatrix} \cos(\theta_2) & 0 & -\sin(\theta_2) \\ 0 & 1 & 0 \\ \sin(\theta_2) & 0 & \cos(\theta_2) \end{bmatrix}, \quad (1)$$

$$Wz(\theta_3) = \begin{bmatrix} \cos(\theta_3) & \sin(\theta_3) & 0 \\ -\sin(\theta_3) & \cos(\theta_3) & 0 \\ 0 & 0 & 1 \end{bmatrix}.$$

The matrices after the conversion of the m and n systems are set to S_n^m, and we can get

$$S_n^m = \begin{bmatrix} \cos\theta_2\cos\theta_3 & \cos\theta_2\cos\theta_3 & -\sin\theta_2 \\ -\cos\theta_3\sin\theta_3 + \sin\theta_1\sin\theta_2\cos\theta_3 & \cos\theta_1\cos\theta_3 + \sin\theta_1\sin\theta_2\sin\theta_3 & \sin\theta_1\cos\theta_2 \\ \sin\theta_1\sin\theta_3 + \cos\theta_1\sin\theta_2\cos\theta_3 & -\sin\theta_1\cos\theta_3 + \cos\theta_1\sin\theta_2\sin\theta_3 & \cos\theta_1\cos\theta_2 \end{bmatrix}. \quad (2)$$

Figure 5: Circuit diagram of UAV PPM decoding module.

Using the quaternion method to express the position of the corners between the two systems. If the drone rotates at a fixed point, the quaternion is set to Q, and the model used to indicate the size of the quaternion is

$$||Q||_2 = Q_0{}^2 + Q_1{}^2 + Q_2{}^2 + Q_3{}^2. \tag{3}$$

Let u be equal to the unit vector. At $||Q|| = 1$时, the quaternion triangle is $Q = \cos(\theta_2/2) + u \sin(\theta_2/2)$, and its exponential form is $Q = m^{u\theta_2/2}$. Then use the quaternion to represent the transformation matrix:

$$S_n^m = \begin{bmatrix} 1 - 2(Q_2{}^2 + Q_3{}^2) & 2(Q_1 Q_2 - Q_0 Q_3) & 2(Q_1 Q_3 + Q_0 Q_2) \\ 2(Q_1 Q_2 + Q_0 Q_3) & 1 - 2(Q_1{}^2 + Q_3{}^2) & 2(Q_2 Q_3 - Q_0 Q_1) \\ 2(Q_1 Q_3 - Q_0 Q_2) & 2(Q_2 Q_3 + Q_0 Q_1) & 1 - 2(Q_1{}^2 + Q_2{}^2) \end{bmatrix}. \tag{4}$$

The value of Euler angle obtained from the conversion matrix is as follows:

$$\begin{aligned} \text{Roll angle}: \theta_1 &= -\arctan \frac{S_m^n(2,3)}{S_m^n(3,3)}, \\ \text{Pitch angle}: \theta_1 &= -\arctan \frac{S_m^n(2,3)}{S_m^n(3,3)}, \\ \text{Yaw angle}: \theta_3 &= -\arctan \frac{S_m^n(1,2)}{S_m^n(1,1)} \end{aligned} \tag{5}$$

In the same way, when we know the initial attitude angle, we can know the quaternion of attitude calculation:

$$Q(0) = \begin{bmatrix} \cos \dfrac{\theta_2(0)}{2} \cos \dfrac{\theta_1(0)}{2} \cos \dfrac{\theta_3(0)}{2} + \sin \dfrac{\theta_2(0)}{2} \sin \dfrac{\theta_1(0)}{2} \sin \dfrac{\theta_3(0)}{2} \\ \sin \dfrac{\theta_2(0)}{2} \cos \dfrac{\theta_1(0)}{2} \cos \dfrac{\theta_3(0)}{2} + \cos \dfrac{\theta_2(0)}{2} \sin \dfrac{\theta_1(0)}{2} \sin \dfrac{\theta_3(0)}{2} \\ \cos \dfrac{\theta_2(0)}{2} \sin \dfrac{\theta_1(0)}{2} \cos \dfrac{\theta_3(0)}{2} - \sin \dfrac{\theta_2(0)}{2} \cos \dfrac{\theta_1(0)}{2} \sin \dfrac{\theta_3(0)}{2} \\ \cos \dfrac{\theta_2(0)}{2} \cos \dfrac{\theta_1(0)}{2} \sin \dfrac{\theta_3(0)}{2} - \sin \dfrac{\theta_2(0)}{2} \sin \dfrac{\theta_1(0)}{2} \cos \dfrac{\theta_3(0)}{2} \end{bmatrix}. \tag{6}$$

2.2.2. Complementary Filtering Algorithm.

Letting the accelerometer measured value at a certain moment be $a^n = [a_x{}^n a_y{}^n a_z{}^n]^t$, and the normalized acceleration is $a^n = [a_x{}^n a_y{}^n a_z{}^n]^t$, the angular velocity of the three-axis gyroscope is $a^n = [a_x{}^n a_y{}^n a_z{}^n]^t$, the vector of gravitational acceleration in the m system is $a^m = [0 0 g]^t$, and the normalized vector is $Am = [0 0 1]$. At the same time, the quaternion value is $Q = [Q_0 Q_1 Q_2 Q_3]t$, ignoring its own acceleration error, and its attitude conversion matrix is

$$S_n^m = \begin{bmatrix} 1 - 2(Q_2{}^2 + Q_3{}^2) & 2(Q_1 Q_2 - Q_0 Q_3) & 2(Q_1 Q_3 + Q_0 Q_2) \\ 2(Q_1 Q_2 + Q_0 Q_3) & 1 - 2(Q_1{}^2 + Q_3{}^2) & 2(Q_2 Q_3 - Q_0 Q_1) \\ 2(Q_1 Q_3 - Q_0 Q_2) & 2(Q_2 Q_3 + Q_0 Q_1) & 1 - 2(Q_1{}^2 + Q_2{}^2) \end{bmatrix}. \tag{7}$$

The normalized acceleration is

$$\begin{aligned} V^n &= \begin{bmatrix} V_x^n \\ V_y^n \\ V_z^n \end{bmatrix} = S_x^n A^m \\ &= \begin{bmatrix} 1 - 2(Q_2{}^2 + Q_3{}^2) & 2(Q_1 Q_2 - Q_0 Q_3) & 2(Q_1 Q_3 + Q_0 Q_2) \\ 2(Q_1 Q_2 + Q_0 Q_3) & 1 - 2(Q_1{}^2 + Q_3{}^2) & 2(Q_2 Q_3 - Q_0 Q_1) \\ 2(Q_1 Q_3 - Q_0 Q_2) & 2(Q_2 Q_3 + Q_0 Q_1) & 1 - 2(Q_1{}^2 + Q_2{}^2) \end{bmatrix}^t \begin{bmatrix} 0 \\ 0 \\ 1 \end{bmatrix}. \end{aligned} \tag{8}$$

At this time, $Vn = An$. Due to the error, the obtained quaternion value is not accurate and can only be an estimated value. Therefore, at this time, the matrix has a rotation angle caused by the error between the actual value of the quaternion and the estimated value. The accuracy of the quaternion value is adjusted to make it infinitely close to the true value. At this time, it can be represented by a vector. Letting the error between Vn and An be Cn, then

$$
\begin{aligned}
C^n &= A^n \times V^n \\
&= \left[A_y{}^n V_z{}^n - A_z{}^n V_y{}^n A_z{}^n V_x{}^n - A_x{}^n V_z{}^n A_x{}^n V_y{}^n - A_y{}^n V_x{}^n \right]^t.
\end{aligned}
\tag{9}
$$

Because $|C^n| = |A^n \times V^n|$ is the angle between the two vectors, Cn is used as the axis of rotation between the vectors, that is, rotating around this axis of rotation can make the two vectors coincide, that is, eliminate the error, and make the quaternion get the true value. Because the quaternion can meet the following conditions:

$$
\frac{dQ}{dT} = \frac{1}{2}\Omega Q = \begin{bmatrix} 0 & -g_x & -g_y & -g_z \\ g_x & 0 & g_z & g_y \\ g_y & -g_z & 0 & g_x \\ g_z & g_y & -g_x & 0 \end{bmatrix} \begin{bmatrix} Q_0 \\ Q_1 \\ Q_2 \\ Q_3 \end{bmatrix}.
\tag{10}
$$

Therefore, the vector rotation axis can be used to correct the gyroscope's angular velocity Gn, so that the attitude angle can get the accurate and true value. The angular velocity after acceleration correction is

$$
G^N = G^n + K_i E^n.
\tag{11}
$$

The error decreases with the correction of the angle, and its attitude angle is constantly changing. The adjustable coefficient of Ki refers to the pushing force of the acceleration on the vector rotation axis. The greater the Ki value, the greater the acceleration pushing force. After correction, a steady-state error will be generated, which can be adjusted by error integration:

$$
E_{JK}^n = E_{JK-1}^n + Kj E_J^n \Delta T.
\tag{12}
$$

E_{JK}^n represents the current error integral, E_{JK-1}^n represents the previous error integral, Ki is the integral coefficient, ΔT is the two time interval, and the final angle can be calculated by this formula:

$$
G_J^N = G^N + E_J^n = G^n + K_i E^n + E_J^n = \left[G_x G_y G_z \right].
\tag{13}
$$

It can be obtained that the quaternion differential equation after acceleration correction is

$$
\frac{dQ}{dT} = \frac{1}{2}\Omega Q = \begin{bmatrix} 0 & -G_x & -G_y & -G_z \\ G_x & 0 & G_z & G_y \\ G_y & -G_z & 0 & G_x \\ G_z & G_y & -G_x & 0 \end{bmatrix} \begin{bmatrix} Q_0 \\ Q_1 \\ Q_2 \\ Q_3 \end{bmatrix}.
\tag{14}
$$

It can be seen that the quaternion solution is

$$
Q(Tk) \left[\exp \frac{1}{2} \int_{k-1}^{k} \Omega dT \right].
\tag{15}
$$

Taking into account the accuracy of the calculation and the speed of the algorithm, this article combines the fourth-order Runge-Kutta method to find the above results. The fourth-order Runge-Kutta method is a high-precision single-step algorithm widely used in engineering, including the famous Euler method, which is used to numerically solve differential equations. Due to the high accuracy of this algorithm, measures are taken to suppress errors, so its implementation principle is also more complicated. The specific steps are

$$
\begin{aligned}
K_1 &= \frac{1}{2}\Omega(T)Q(T), \\
K_2 &= \frac{1}{2}\Omega\left(T + \frac{t}{2}\right)Q\left(T + \frac{K_1 t}{2}\right), \\
K_3 &= \frac{1}{2}\Omega\left(T + \frac{t}{2}\right)Q\left(T + \frac{K_2 t}{2}\right), \\
K_4 &= \frac{1}{2}\Omega(T + t)Q(T + K_3 t).
\end{aligned}
\tag{16}
$$

It can be seen that the updated value of the obtained quaternion is

$$
Q(T + t) = Q(T) + \frac{t}{6}(K_1 + 2K_2 + 2K_3 + 2K_4).
\tag{17}
$$

T is the calculation step length of the attitude calculation. The magnetic field strength can be measured by a magnetometer, and the component of the geomagnetic field strength can be estimated according to the estimated attitude angle and the characteristics of the geomagnetic field. In the complementary filtering algorithm, the error decreases with the correction of the angle, and its attitude angle also changes continuously. At this time, the difference between measuring the magnetic field strength with a magnetic field meter and the acceleration correction angular velocity is that we do not know the component value of the magnetic field in the earth coordinate system. Measuring the magnetic field intensity in the UAV coordinate system by a magnetic field meter: set $h^n = [h_x{}^n h_y{}^n h_z{}^n]^t$, and get $H^n = [H_x{}^n H_y{}^n H_z{}^n]^t$ after normalization. After the geomagnetic field is transformed by the attitude transformation matrix, we can get

$$H^m = \begin{bmatrix} H_x^m \\ H_y^m \\ H_z^m \end{bmatrix} = S_n^m H^n. \tag{18}$$

Supposing the normalized magnetic field intensity is $F^m = [F_x^m 0 F_z^m]^t$, we know that $F_x^m = \sqrt{(H_x^m)^2 + (H_y^m)^2}$, the geomagnetic field obtained by the quaternion method can be calculated as

$$
\begin{aligned}
F^n &= \begin{bmatrix} F_x^n \\ F_y^n \\ F_z^n \end{bmatrix} = S_m^n F^m \\
&= \begin{bmatrix} 1 - 2\left(Q_2^2 + Q_3^2\right) & 2(Q_1 Q_2 - Q_0 Q_3) & 2(Q_1 Q_3 + Q_0 Q_2) \\ 2(Q_1 Q_2 + Q_0 Q_3) & 1 - 2\left(Q_1^2 + Q_3^2\right) & 2(Q_2 Q_3 - Q_0 Q_1) \\ 2(Q_1 Q_3 - Q_0 Q_2) & 2(Q_2 Q_3 + Q_0 Q_1) & 1 - 2\left(Q_1^2 + Q_2^2\right) \end{bmatrix}^t \begin{bmatrix} F_x^n \\ 0 \\ F_z^n \end{bmatrix}.
\end{aligned}
\tag{19}
$$

The error between the two vectors is

$$
\begin{aligned}
E_h^n &= H^n \times F^n \\
&= \left[H_y^n H_z^n - H_z^n H_y^n \ H_z^n H_x^n - H_x^n H_z^n \ H_x^n H_y^n - H_y^n H_x^n \right]^t.
\end{aligned}
\tag{20}
$$

This method can correct errors and obtain accurate values.

2.3. Wireless Communication Propagation Model for Smart Farmland Monitoring. Radio is used in many fields and has different requirements in each field. Therefore, different radio propagation models and electromagnetic coverage characteristics are arranged according to their needs. Plasma can cover the electromagnetic properties of the object. And based on the UAV smart farmland information monitoring system, there is naturally a corresponding radio model, because the collection point is located in the field farmland, after screening, the Egli model is the most suitable choice, which can perform well in plains, hills, farmland, and mountains [11]. Prior to this, build a smart farmland information monitoring system based on UAV system, as shown in Figure 6.

2.3.1. Free Space Propagation Model and Egli Model. The free space model means that the electromagnetic wave is stable and lossless during the propagation process, there is no obstacle interference, only the electromagnetic wave loss attenuation formed during diffusion, but this model is only in an ideal state, and the conditions that affect the signal include transmission frequency, transmission power, interference electromagnetic wave intensity, receiver sensitivity, and gain coefficient. Taking different propagation frequencies as an example, in the free space model, under certain conditions, the electromagnetic wave signal will be greatly attenuated, which is positively correlated with the propaga-

tion distance. That is, the distance will affect the propagation loss, so we can observe the path loss under different propagation distances [12].

The Egli model is able to enhance the propagation strength and is mainly applied to VHF and UHF, where there is a state of ultrashort wave. This model can be used extremely well in plains, hills, farmland, and mountains, and the effect is significantly improved compared with other models [13]. Its propagation distance is positively correlated with the path loss of the same frequency band. The comparison between the two models is shown in Figure 7.

It can be seen that the LM based on the Egli model is obviously larger than the free-space propagation model, that is, the Egli model is more accurate in measurement, let alone in the wild geographic environment.

3. Static Simulation Experiment of Different Tail Drive Systems of Single-Rotor Agricultural UAV

The single-rotor UAV has the characteristics of fast and light, single-rotor UAVs have large rotors, are more stable, have good wind resistance, and have better-operating results. Although the cost of a multirotor is lower than that of a single-rotor, it has not been widely promoted due to its instability, poor wind resistance, and poor operational ability due to its own rotor. It has considerable utility in the construction and control of smart farms. It can measure humidity, wirelessly sense, control temperature, avoid vegetation, spray pesticides, etc. It also excels in mountain and plain survey, vegetation disease monitoring, and animal monitoring. In this experiment, two types of tail transmission systems are built, their dynamic characteristics are tested, and experiments are carried out to prove the optimized effect [14]. Analyzing its stress, strain, and vibration distribution rules, test the bevel gear and the fixed shaft of the tail rotor, and the transmission load condition of the single-rotor agricultural UAV, compare the material performance, and whether it can operate normally under the damaged condition [15].

3.1. Establishment of Finite Element Model. Among the statics analysis methods, the establishment of finite element models is widely used, and the FEA (finite element analysis) has the characteristics of high efficiency and extensiveness. Based on computer numerical analysis, it simulates physical problems, divides and solves related obstacles, using the simulation plug-in in SolidWork to realize piping design, feature recognition, model testing, appearance rendering, dynamic simulation, and finite element model construction and analysis of the designed model. SolidWork has 3D Instant Website, CircuitWorks(TM), and other plug-ins. The advantage of the simulation plug-in is that it can achieve the purpose of optimizing design or reducing weight. Using simulation modeling to integrate the simulation interface and process into the SolidWork construction, and the strength, stiffness, and path loss of the tail of the single-rotor agricultural UAV in the smart farm can be tested and optimized for the frequency, performance weakening, buckling stability, and thermal conductivity, to make its performance more and
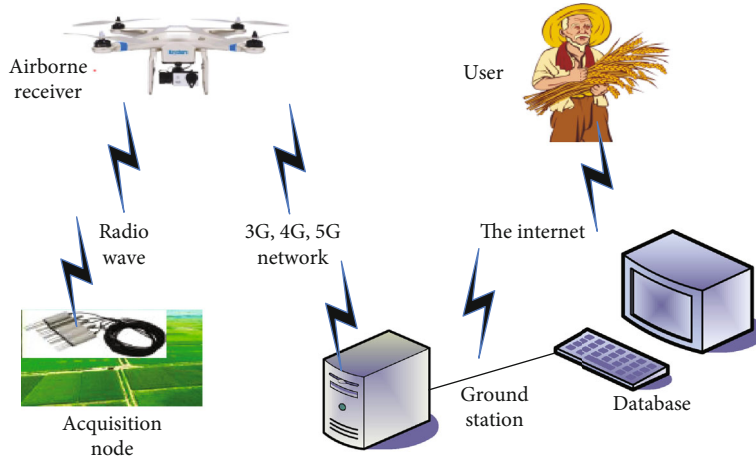
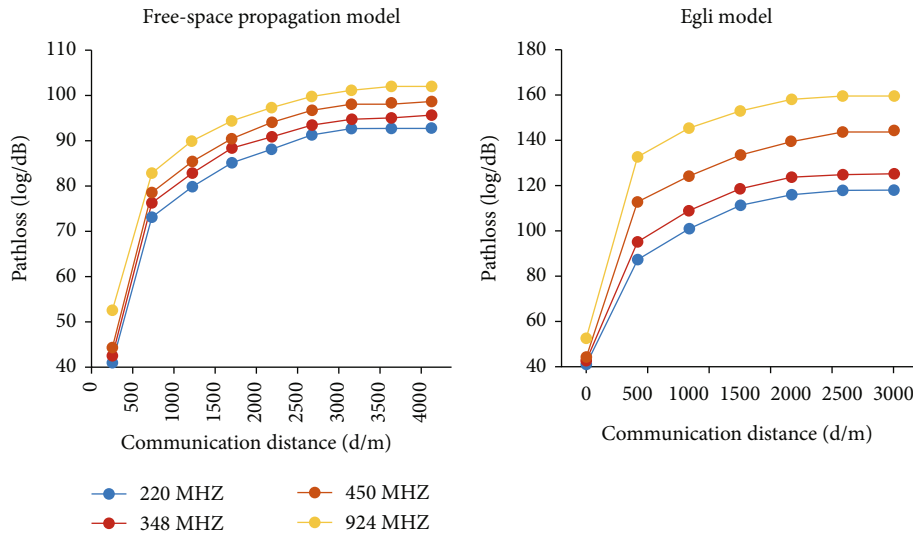FIGURE 6: Smart farmland information monitoring system based on UAV system.

FIGURE 7: Free space propagation model and Egli model path loss at each frequency.

more perfect, its analysis includes preprocessing, solving, and postprocessing [16].

First, establishing two finite element models, namely, the synchronous belt tail drive system model and the bevel gear tail drive system model. The former has a tail rotor fixed shaft, while the bevel gear tail drive system model is constructed with a bevel gear as an external package structure. The horizontal drive shaft is set to a shaft diameter of 6 mm and a fixed shaft of the tail rotor of 2 mm, the fixed shaft of the tail rotor and the bevel gear tail transmission system have the same settings except for the length and other parameters, and the length of the fixed shaft of the 2 mm tail rotor does not affect its mechanical performance. Therefore, when establishing the finite element model, the bevel gear tail transmission system only needs to test the performance of the bevel gear [17]. Observing the statics data of the synchronous belt tail transmission system under different loads. At this time, let $T = 0.024$ N.m, $T = 0.036$ N.m, and $T = 0.048$ N.m, T is the acting torque under the force of the synchronous pulley, in this state, it can be obtained that

when $T = 0.024$ N.m, the timing belt pulley is the largest, and its stress distribution appears at the transition between the toothed structure and the pulley. Fmax, the maximum stress can be measured as 22.4 MPa, Pmax, the maximum strain can be obtained as $1.60 * 10 - 4$, the minimum safety factor is 8.18, taking the stress points around this wheel and summarize the driving distances. The results are shown in Table 1.

T is the acting torque under the force of the synchronous belt wheel. In this state, it can be obtained that when $T = 0.036$ N.m, the synchronous belt wheel is the largest, and its stress distribution appears at the transition between the toothed structure and the belt wheel. Fmax, the maximum stress can be measured as 41.9 MPa, Pmax, the maximum strain can be obtained as $2.16 * 10 - 4$, and the minimum safety factor is 5.73. Taking the stress points around this wheel and summarize the travel distance. The results are as follows in Table 2.

T is the acting torque under the force of the synchronous belt wheel. In this state, it can be obtained that when

TABLE 1: Timing pulley point position when torque $T = 0.024$ N.m.

Take the number of the node	A	B	C	Displacement/mm
270239	0.578021	1.60524	3.879813	1.56E-03
987	0.916311	-5.31679	4.045005	1.29E-03
275210	-1.810324	0.59162	3.925177	1.42E-03
271006	-1.599076	4.44148	4.192814	1.24E-03
1192	-0.336402	-5.54489	3.744727	7.12E-04
256139	5.279374	3.40041	3.792044	2.99E-04
254959	3.19446	-2.98182	4.159314	8.47E-04
270828	5.234079	-5.56402	3.90418	1.34E-03
259627	1.843191	3.27218	4.022577	1.25E-03
270264	5.419277	-0.71241	4.098225	1.40E-03
256408	-2.677982	0.19545	4.001304	1.78E-03

TABLE 2: The position of the timing belt wheel point when the torque $T = 0.036$ N.m.

Take the number of the node	A	B	C	Displacement/mm
271854	3.349839	6.87772	3.970724	2.46E-03
271869	3.216285	4.56171	4.0148	2.31E-03
1075	-3.695157	-5.53452	4.191693	2.12E-03
1065	6.33761	-2.21191	4.127614	1.77E-03
1122	-2.964771	-0.12905	4.047418	1.96E-03
1098	7.3054	3.49538	4.046982	1.17E-03
1114	0.327336	3.26831	3.945255	9.02E-04
270707	-2.060536	-1.36653	4.01843	5.73E-04
4169	-3.599715	2.28391	4.149825	1.88E-03
258643	0.110075	0.07336	4.155801	2.08E-03
258655	-3.740832	-4.40821	4.155786	2.33E-03

TABLE 3: Timing pulley point position when torque $T = 0.048$ N.m.

Take the number of the node	A	B	C	Displacement/mm
271736	-4.484425	5.17246	3.915899	2.92E-03
270875	-2.197064	2.75294	3.901097	2.71E-03
271576	3.420842	-1.62045	3.702177	2.18E-03
271373	-1.555312	5.31437	3.847285	5.12E-04
271253	4.442686	-1.83356	3.881204	9.27E-04
270259	-0.903076	4.16805	4.132725	1.21E-03
271001	1.593243	-6.14098	4.004139	2.53E-03
3956	-1.832493	1.82812	4.133907	2.36E-03
3981	3.310991	-6.2738	4.03869	2.78E-03
270122	3.633055	-4.63785	4.099114	2.84E-03
1072	5.922262	5.08424	3.806407	2.77E-03

related point. Fmax, the maximum stress can be measured as 11.49 MPa, Pmax, the maximum strain can be obtained as $3.74 * 10 - 5$, the minimum safety factor is 15.48. When the torque of the fixed shaft of the tail rotor is $T = 0.048$ N.m, the maximum point of the timing belt wheel will appear at the point of interference between the fixed shaft of the tail rotor and the timing belt wheel, or at one end of the fixed point of the tail rotor and its related point. Fmax, the maximum stress can be measured as 15.11 MPa, Pmax, the maximum strain can be obtained as $4.97 * 10 - 5$, and the minimum safety factor is 12.11. The strain diagrams under three different conditions are shown in Figure 8.

3.2. Statics Experiment of the Bevel Gear Tail Transmission System of the Smart Farm Drone under Different Loads. In the case of controlling other attributes, set the acting torque of the bevel gear as a variable, and then analyze the distribution state of the force points at the three torques [18]. The strain distribution comparison chart can be obtained as shown in Figure 9.

It can be observed that the strain curve changes in the three states. At torque $T = 0.024$ N.m, the maximum stress is located at the junction of the two gears. At this time, the maximum stress Fmax, that is, the maximum stress, can be measured as 42.96 MPa. The maximum strain in this case is $1.17 * 10 - 4$, and the safety factor is 11.12. At torque $T = 0.036$ Nm, the maximum stress is at the junction of the two gears. At this time, the maximum stress Fmax, that is, the maximum stress can be measured as 56.6 MPa. The maximum strain in this case is $1.82 * 10 - 4$, and the safety factor is 8.41. At torque $T = 0.048$ Nm, the maximum stress is at the junction of the two gears. At this time, the maximum stress Fmax, that is, the maximum stress can be measured as 73.8 MPa. The maximum strain in this case is $2.41 * 10 - 4$, and the safety factor is 6.27. The material used is high-performance carbon nanostructured steel. The required stress for this type of steel is 89.2 N.mm2, 72.6 MPa, and the steel used is no. 40 steel, which shows that it can meet the demand.

At torque $T = 0.024$ N.m, the maximum stress is located at the junction of the two gears. At this time, the maximum stress Fmax, that is, the maximum stress can be measured as

$T = 0.048$ N.m, the synchronous belt wheel is at its maximum, and its stress distribution appears at the transition between the toothed structure and the belt wheel. Fmax, the maximum stress can be measured as 54.6 MPa, Pmax, the maximum strain can be obtained as $2.68 * 10 - 4$, and the minimum safety factor is 4.26. Taking the stress points around the wheel and summarize the travel distance. The results are as follows Table 3.

When the torque of the fixed shaft of the tail rotor is $T = 0.024$ N.m, the maximum stress of the tail rotor will change. The maximum point will appear at the point of interference between the fixed shaft of the tail rotor and the timing pulley, or at one end of the fixed point of the tail rotor and its related point. Fmax, the maximum stress can be measured as 8.68 MPa, Pmax, the maximum strain can be obtained as $2.78 * 10 - 5$, the minimum safety factor is 14.77. When the torque of the fixed shaft of the tail rotor is $T = 0.036$ N.m, the maximum point of the timing belt wheel will appear at the point of interference between the fixed shaft of the tail rotor and the timing belt wheel, or at one end of the fixed point of the tail rotor and its
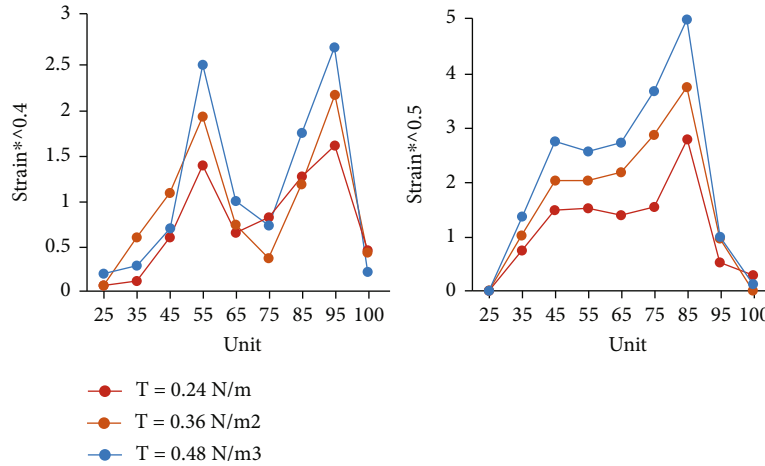
Figure 8: Point strain distribution in the axial direction based on the transition between the synchronous pulley and the pulley and the fixed shaft of the tail rotor.
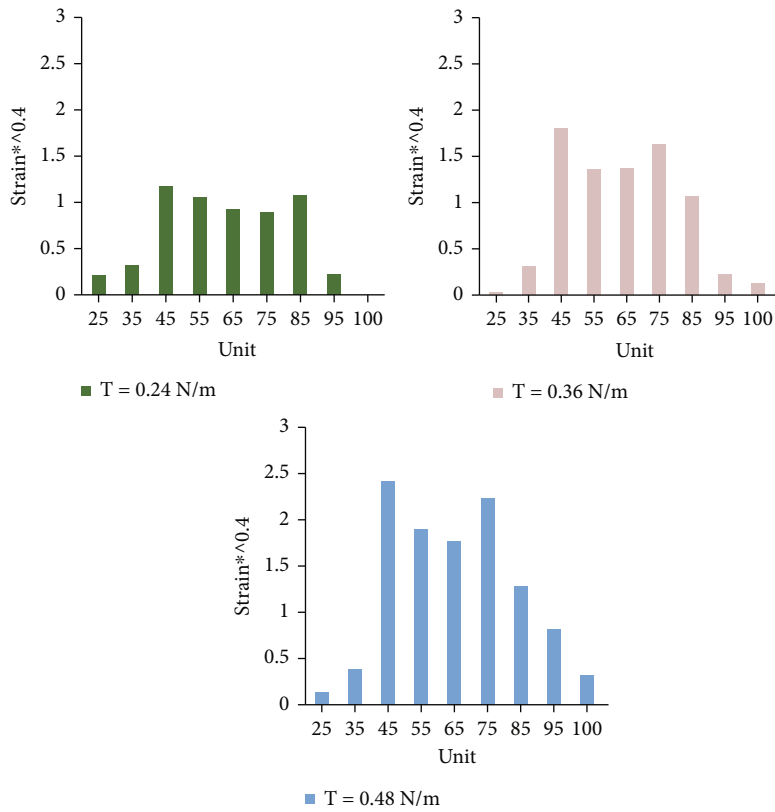

Figure 9: Strain relationship under three torques: $T = 0.024$ N.m, $T = 0.036$ N.m, and $T = 0.048$ N.m.

42.96 MPa. The maximum strain in this case is $1.17 * 10 - 4$, and the safety factor is 11.12. At torque $T = 0.036$ Nm, the maximum stress is at the junction of the two gears. At this time, the maximum stress Fmax, that is, the maximum stress can be measured as 56.6 MPa. The maximum strain in this case is $1.82 * 10 - 4$, and the safety factor is 8.41. At torque $T = 0.048$ Nm, the maximum stress is at the junction of the two gears. At this time, the maximum stress Fmax, that is, the maximum stress can be measured as 73.8 MPa. The max-

imum strain in this case is $2.41 * 10 - 4$, and the safety factor is 6.27. At this time, the high-performance steel required for the fixed shaft of the tail rotor is 113.8 N.mm^2 and 14.85 MPa, which can also meet the requirements.

3.3. Comparison of Statics Analysis of Tail Transmission System under Different Drives. In order to further test the mechanical characteristics of the transmission system of the single-rotor agricultural UAV in the smart farm, prepare
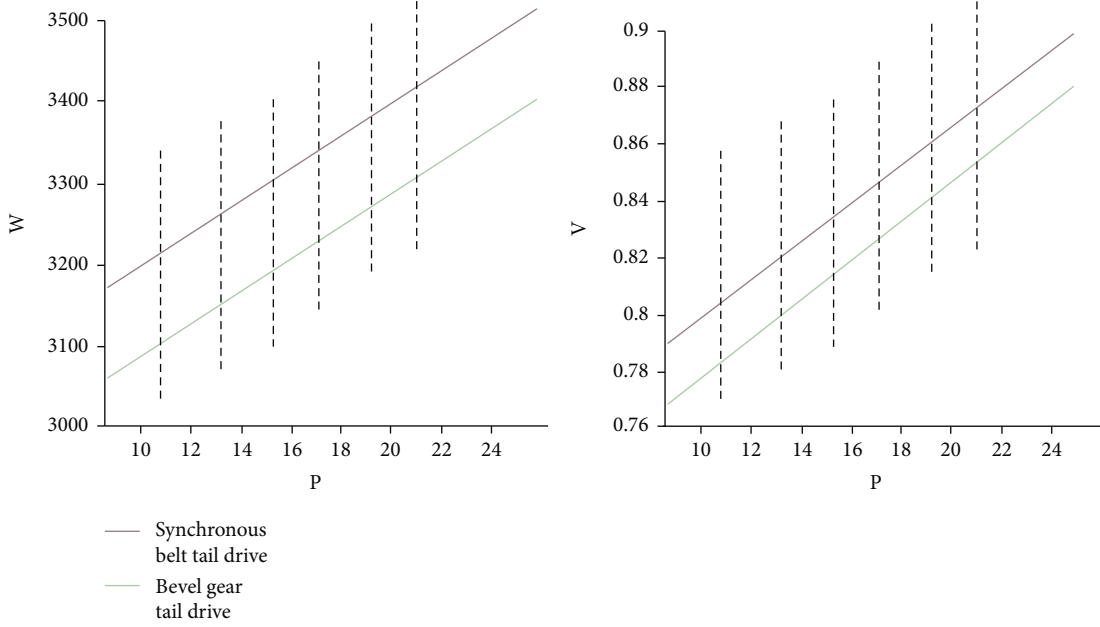
FIGURE 10: Power and speed fitting and power and wind speed fitting of synchronous belt tail drive system and bevel gear tail drive system, the former is speed fitting, and the latter is wind speed fitting.

its dynamic test experiment, the experiment prepared a push-button power switch, stable output voltage 220 V, output current 1A-100A, power regulator, used sensor noncontact wireless measurement, the measured distance is 50-300 mm, and the hand-held small wind speed measuring instrument, the measured range is 0.4-36 m/s, and the measurement may have an error value within the range of 2% before and after [19]. Using the digital tachometer to measure the rotational speed s (r/min) of the fixed shaft of the tail rotor, so that each group of experimental data can be measured into 6 groups. At a certain rotational speed and power, Figure 10 can be obtained.

The power and speed fitting results of the synchronous belt tail drive system show $W = 31.22P + 2843$, the standard deviation is 32.02, and the fitting function coincidence degree is 0.9276, the value is high, close to 1. Through these 6 sets of data, the display power and wind speed fitting result is $V = 0.01014 + 0.6701$, the standard deviation is 0.1092, the fitting function coincidence degree is 0.9302, and the same value is large, close to 1 [20]. The fitting result of the power and speed of the bevel gear transmission system shows $W = 29.52P + 2754$, the standard deviation is 28.61, the coincidence degree of the fitting function is 0.9431, the value is high, close to 1. Through these 6 sets of data, it is shown that the power and wind speed fitting result is $V = 0.009851 + 0.6522$, the standard deviation is 0.01023, and the fitting function coincidence degree is 0.9328, the same value is large, close to 1.

The result of this experiment is that the fitting value of the power and speed of the synchronous belt tail transmission system is 31.22, and under the same conditions, the fitting value of the bevel gear is 29.52, an increase of 5.76% compared to the same period last year. After comparing the power, torque, and speed, it can be calculated that under

load conditions, the fitting value of the transmission power and wind speed of the synchronous belt tail is 0.01014, while the fitting value of the bevel gear is 0.009851, an increase of 2.93% compared to the same period last year. It can be concluded that the bevel gear tail drive system has higher dynamic characteristics than the tail rotor reaction force of the synchronous belt tail drive system. When it is applied to the smart construction farm, the bevel gear tail drive system can be used.

4. Discussion

This article focuses on the application of single-rotor UAVs and multirotor UAVs in smart construction farms and the UAV dynamics performance, algorithm, structure, circuit structure, and use experiments to test the dynamic characteristics of the tail rotor reaction force of the bevel gear tail transmission system compared with the synchronous belt tail transmission system. This plays a certain guiding role in the application of the bevel gear tail transmission system of the single-rotor agricultural UAV to the farm [21]. Its stress-strain and other characteristics can be applied to the design of agricultural drones. This article first outlines smart farms and drones and then describes the method of designing drone circuits. The minimum UAV circuit design includes the UAV reset circuit, UAV crystal oscillator circuit, UAV upgrade circuit and UAV PPM decoding module circuit diagram, backup monitoring function, and other parts capable of signal monitoring, to change the line opening and closing state, change the line at any time to improve the safety of the UAV system, then explain the attitude calculation and complementary filtering of the multiwing UAV. The calculation process combines inertial navigation and sensor data fusion. The complementary filtering

algorithm is applied to the attitude calculation, and the two sensors can be selected and discarded. Using the coordinate system to analyze the quaternion method and Euler angle calculation, through the conversion matrix, minimize the error. Then establish a wireless communication propagation model for smart farmland monitoring, which is mainly applied to the state where VHF and UHF have ultrashort waves. The LM based on the Egli model is obviously larger than the free space propagation model, that is, the Egli model is more accurate in measurement, let alone in the field geographic environment [22]. After that, the static performance of different tail transmission systems of single-rotor agricultural UAVs was tested, and two tail transmission systems were built. Studying and analyzing the changes of strain curve under different loads through finite element analysis under the conditions of production of no. 40 steel. According to different stress points, the power and speed fitting of the synchronous belt tail drive system and the bevel gear tail drive system and the power and wind speed fitting are carried out. In contrast, the power and speed of the synchronous belt tail drive are 5.76% more than that of the bevel gear. After comparing the power, torque, and speed, it can be calculated that under load conditions, the power and speed of the synchronous belt tail transmission are 2.93% more than that of the bevel gear. It can be seen that in the construction of farms, the use of bevel gear tail transmission undoubtedly has better performance. It can have good response capabilities when flying a single-rotor UAV or when avoiding obstacles, so as to ensure the safety of the UAV system.

5. Conclusions

For the static simulation experiment of different tail drive systems for single-rotor agricultural UAVs, it can be seen that under the same conditions, the bevel gear tail drive system has higher dynamic characteristics than the tail rotor reaction force of the synchronous belt tail drive system. When applied to a smart farm, a bevel gear tail transmission system can be used. The fitting value of the power and speed of the synchronous belt tail drive system is 31.22, and the fitting value of the bevel gear is 29.52, an increase of 5.76% compared to the same period last year. After comparing power, torque, and speed, it can be calculated that under load conditions, the fitting value of the transmission power and wind speed of the synchronous belt tail is 0.01014, while the fitting value of the bevel gear is 0.009851, an increase of 2.93% year-on-year. This has a good prospect in the application of smart farms, but there is a little error in the data, which is not too accurate.

Data Availability

The data used to support the findings of this study are available from the corresponding author upon request.

Conflicts of Interest

The authors declare no conflicts of interest.

References

[1] C. E. Tinney and J. Sirohi, "Multirotor drone noise at static thrust," *AIAA Journal*, vol. 56, no. 1468, pp. 1–11, 2018.

[2] V. Semkin, J. Haarla, T. Pairon et al., "Analyzing radar cross section signatures of diverse drone models at mmWave frequencies," *IEEE Access*, vol. 8, no. 99, 2020.

[3] C. C. Chang, C. Y. Chang, J. L. Wang et al., "A study of atmospheric mixing of trace gases by aerial sampling with a multi- rotor drone," *Atmospheric Environment*, vol. 184, pp. 254–261, 2018.

[4] I. B. Mabrouk and A. El Hami, "Dynamic response analysis of Darrieus wind turbine geared transmission system with unsteady wind inflow," *Renewable Energy*, vol. 131, pp. 482–493, 2019.

[5] T. Kawai, S. Kaneda, L. Takai, and H. Mineno, "A virtual WLAN device model for high-fidelity wireless network emulation," *Simulation*, vol. 27, no. 3, pp. 1–24, 2017.

[6] S. Saadaoui, M. Tabaa, F. Monteiro, M. Chehaitly, and A. Dandache, "Discrete wavelet packet transform-based industrial digital wireless communication systems," *Information*, vol. 10, no. 3, pp. 104–104, 2019.

[7] B. Zhou, W. Tu, K. Mai, W. Xue, W. Ma, and Q. Li, "A novel access point placement method for WiFi fingerprinting considering existing APs," *IEEE Wireless Communication Letters*, vol. 9, 2020.

[8] J. Calleja, "Near Miss Between Drone and Ag Aircraft in Iowa an Eye-Opener," *Agricultural aviation*, vol. 44, no. 4, pp. 62–64, 2017.

[9] C. J. Chen, Y. Y. Huang, Y. S. Li, Y. C. Chen, C. Y. Chang, and Y. M. Huang, "Identification of fruit tree pests with deep learning on embedded drone to achieve accurate pesticide spraying," *IEEE Access*, vol. 9, 2021.

[10] N. Ishitsuka, N. Iwasaki, and T. Sakamoto, "Unevenness measurement of damaged paddy rice fields by the Kumamoto earthquake using multicopper type UAV and factor investigation of the unevenness damage outbreak," *Journal of the Japanese Agricultural Systems Society*, vol. 34, no. 2, pp. 41–47, 2018.

[11] H. F. Abou-Shaara, "Using safe materials to control _Varroa_ mites with studying grooming behavior of honey bees and morphology of _Varroa_ over winter," *Annals of Agricultural Sciences*, vol. 62, no. 2, pp. 205–210, 2017.

[12] S. Nagai, T. M. Saitoh, K. Kajiwara, S. Yoshitake, and Y. Honda, "Investigation of the potential of drone observations for detection of forest disturbance caused by heavy snow damage in a Japanese cedar (<I>Cryptomeria japonica</I>) forest," *Journal of Agricultural Meteorology*, vol. 74, no. 3, pp. 123–127, 2018.

[13] P. A. Tassi, S. Rhebergen, C. A. Vionnet, and O. Bokhove, "A discontinuous Galerkin finite element model for river bed evolution under shallow flows," *Computer Methods in Applied Mechanics & Engineering*, vol. 197, no. 33-40, 2018.

[14] B. Hanson, "A fully three-dimensional finite-element model applied to velocities on Storglaciären, Sweden," *Journal of Glaciology*, vol. 41, no. 137, pp. 91–102, 1995.

[15] G. Park, T. Kim, M. B. Panzer, and J. R. Crandall, "Validation of shoulder response of human body finite-element model (GHBMC) under whole body lateral impact condition," *Annals of Biomedical Engineering*, vol. 44, no. 8, pp. 2558–2576, 2016.

[16] B. Philippe, S. S. Bruce, and S. S. Da, "Updating of a nonlinear finite element model using discrete-time Volterra series," *Latin American Journal of Solids & Structures*, vol. 14, no. 7, pp. 1183–1199, 2017.

[17] T. Schloegl and S. Leyendecker, "Electrostatic-viscoelastic finite element model of dielectric actuators," *Computer Methods in Applied Mechanics & Engineering*, vol. 299, pp. 421–439, 2016.

[18] Q. Q. Yang, L. L. Sun, and L. Yang, "A fast adaptive-gain complementary filter algorithm for attitude estimation of an unmanned aerial vehicle," *The Journal of Navigation*, vol. 71, no. 6, pp. 1478–1491, 2018.

[19] C. J. Labuzzetta, M. L. Antonio, P. M. Watson et al., "Complementary feature selection from alternative splicing events and gene expression for phenotype prediction," *Bioinformatics*, vol. 32, no. 17, pp. i421–i429, 2016.

[20] J. Madeiras, C. Cardeira, and P. Oliveira, "Vision-aided complementary filter for attitude and position estimation: design, analysis and experimental validation," *IFAC-PapersOnLine*, vol. 52, no. 12, pp. 388–393, 2019.

[21] A. M. Arthur, R. Arthur, A. G. Silva, M. S. Fouto, Y. Iano, and J. M. L. de Faria, "Algorithm for predicting macular dysfunction based on moment invariants classification of the foveal avascular zone in functional retinal images," *Research on Biomedical Engineering*, vol. 33, no. 4, pp. 344–351, 2017.

[22] H. Zhang, J. Zhu, and Z. Huang, "The Research on Improved Adaptive Complementary Filter Algorithm Based on the AHRS," *Guti Dianzixue Yanjiu Yu Jinzhan/Research and Progress of Solid State Electronics*, vol. 38, no. 2, pp. 141–145, 2018.